Lattice thermal conductivity of TiS$_2$, ZrS$_2$, and HfS$_2$: Periodic trends studied by dispersion-corrected hybrid density functional methods

Nina Glebko and Antti J. Karttunen[*]

Department of Chemistry and Materials Science, Aalto University, P.O. Box 16100, FI-00076 Aalto, Finland

The lattice thermal conductivity of layered group 4 disulfides TiS$_2$, ZrS$_2$, and HfS$_2$ has been studied using dispersion-corrected hybrid density functional methods. Results obtained using both relaxation time approximation (RTA) and full solution of linearized Boltzmann transport equation have been compared and rigorously analyzed. The periodic trends of lattice thermal conductivity and its components are investigated in detail. The in-plane RTA lattice thermal conductivities of TiS$_2$, ZrS$_2$, and HfS$_2$ at 300 K are 6.1, 8.5, and 11.7 W m^{-1} K^{-1}, respectively. In the cross-plane direction, where the metal sulfide layers are kept together by weak van der Waals interactions, the RTA lattice thermal conductivities of TiS$_2$, ZrS$_2$, and HfS$_2$ at 300 K are 1.4, 1.4, and 2.0 W m^{-1} K^{-1}, respectively.

I. INTRODUCTION

Group 4 transition metal disulfides MS$_2$, where M = Ti, Zr, Hf, are semiconductors adopting trigonal, layered CdI$_2$-type structure (space group $P\bar{3}m1$, Fig. 1). The layers parallel to the *ab* plane consist of covalently bound M–S octahedra and they are stacked in the cross-plane *c* direction via weak van der Waals interactions. The weakness of the interlayer interactions enables the tuning of the MS$_2$ structures with intercalation reactions. In such an intercalation approach, guest atoms or molecules are introduced to the interlayer space by using various synthetic techniques. There are a number of studies reporting successful use of TiS$_2$ as a host material for molecular [1,2] and atomic (e.g., Co) [3–6] intercalation. Since TiS$_2$ is a known thermoelectric material that can convert temperature differences into electrical energy, one of the main goals in the intercalations studies has been to improve the thermoelectric efficiency of TiS$_2$.

The thermoelectric efficiency of a material is expressed by dimensionless figure of merit ZT:

$$ZT = \frac{S^2\sigma}{\kappa_l + \kappa_e}T, \tag{1}$$

where S describes Seebeck coefficient (thermopower), σ the electrical conductivity, κ_l the lattice thermal conductivity, κ_e the electronic thermal conductivity, and T the temperature. In solids, heat can be carried by lattice vibrations, phonons (κ_l), and by electrons or holes (κ_e). In insulators and semiconductors, the electronic thermal conductivity is relatively small and can usually be neglected when the goal is to reduce total thermal conductivity. Overall, reducing lattice thermal conductivity while conserving reasonable electrical conductivity is one of the most successful strategies for designing highly efficient thermoelectrics (also known as the phonon glass-electron crystal concept). One of the possible approaches in this direction is to increase the phonon scattering with intercalated organic molecules, thus decreasing the phonon lifetime and reducing the lattice thermal conductivity [7].

Systematic improvement of the intercalated thermoelectric MS$_2$ materials requires that the thermoelectric properties of the parent lattice are well understood. In particular, understanding the lattice thermal conductivity of a material at the atomic level can pinpoint the critical factors that could be modified by intercalation reactions of properly tailored molecular guests. In the case of group 4 disulfides TiS$_2$, ZrS$_2$, and HfS$_2$, the lattice thermal conductivity trends have not been studied systematically.

The majority of studies on the thermoelectric properties of TiS$_2$ describe polycrystalline samples [4,6–10], but studies on TiS$_2$ single crystals have been published as well. Imai *et al.* reported the lattice thermal conductivity of highly stoichiometric TiS$_2$ single crystal to be 6.4 and 4.2 W m^{-1} K^{-1} in the in-plane and cross-plane direction, respectively (at 300 K) [11]. In 2015, Daou *et al.* investigated the effect of substitution and intercalation of metal atoms on the thermoelectric properties of TiS$_2$ and reported in-plane κ_l of about 4.5 W m^{-1} K^{-1} at 275 K [5]. Later, Koumoto *et al.* measured in-plane lattice thermal conductivity to be 4.2 W m^{-1} K^{-1} at 300 K [1].

In the case of ZrS$_2$ and HfS$_2$, the experimental values for κ_l have not been reported, and computational studies have mostly focused on 2D monolayers [12–14]. In 2015, Yumnam *et al.* did investigate the thermoelectric properties of bulk ZrS$_2$ and HfS$_2$ within density functional theory (DFT) and semiclassical Boltzmann transport equation (DFT-TB-mBJ method, using experimental lattice constants) [15] They calculated the total thermal conductivity from $\kappa_l + \kappa_e$ using constant relaxation time approximation. The electronic relaxation time τ was derived by comparing calculated σ/τ with experimental σ for ZrSe$_2$ and assuming τ to be similar in ZrS$_2$ and HfS$_2$. They predicted total thermal conductivities at 300 K to be 17 and 9 W m^{-1} K^{-1} for ZrS$_2$ and HfS$_2$, respectively.
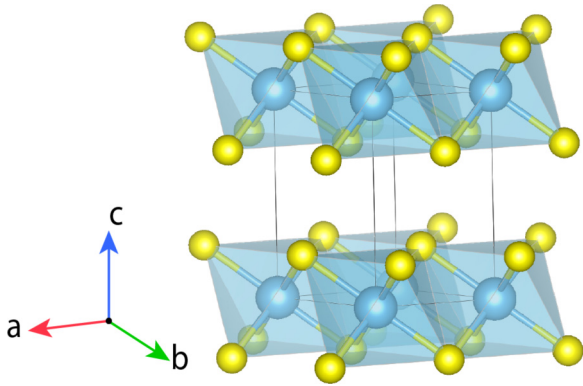
_____

*antti.j.karttunen@iki.fi

FIG. 1. Crystal structure of TiS_2, ZrS_2, and HfS_2. Blue: Metal; yellow: Sulfur.

The electronic contribution was estimated to be only 1–3% of the total thermal conductivity.

To our knowledge, the periodic trends of the lattice thermal conductivity of group 4 disulfides TiS_2, ZrS_2, and HfS_2 have not been studied and explained previously. Here we study the lattice thermal conductivity of TiS_2, ZrS_2, HfS_2 using dispersion-corrected hybrid density functional methods and Boltzmann transport theory. Combining hybrid DFT methods with dispersion corrections enables accurate description of the layered MS_2 compounds with both covalent M–S bonds and weak interlayer interactions. We analyze in detail the physical quantities behind the lattice thermal conductivity to explain the lattice thermal conductivity trends.

II. COMPUTATIONAL DETAILS

The DFT calculations have been done with a development version of the CRYSTAL14 program package [16]. We applied PBE0 hybrid density functional method [17] and Gaussian-type triple-ζ-valence + polarization level basis set (TZVP) [18,19]. In order to take into account the weak interlayer van der Waals interactions, we used the semiempirical D3 dispersion correction developed by Grimme [20,21]. We applied the zero-damping scheme in the dispersion correction as we have previously shown the Becke-Johnson damping to overestimate the interlayer interaction in the studied MS_2 structures [19].

The optimized structures of TiS_2, ZrS_2, and HfS_2 were taken from our previous study, which also includes geometry optimization benchmarks at the applied DFT-PBE0-D3/TZVP level of theory [19]. In the lattice dynamics and thermal conductivity calculations, we applied tight SCF convergence criterion of 10^{-10} a.u. The calculations were mostly carried out with Coulomb and exchange integral tolerance factors (TOLINTEG) set to tight values of 8, 8, 8, 8, and 16, but even tighter values of 9, 9, 9, 9, and 18 were used in the phonon supercell calculations.

The phonon dispersions were calculated within the harmonic approximation using PHONOPY code [22,23]. The second-order force constants and phonon dispersion relations are obtained by calculating forces in supercells with atomic displacements. Previous thermal property studies with quasi-harmonic approximation in CRYSTAL have shown that, if the

unit cell volume changes, high numerical accuracy in phonon properties requires careful consideration of the reference geometry of two-electron integral evaluation (keyword FIXIN-DEX) [24]. However, in the present phonon supercell force calculations, the lattice parameters of all supercells are identical and there is no need to apply the FIXINDEX keyword during the supercell calculations. For ZrS_2 and HfS_2 we used a $3 \times 3 \times 2$ supercell and atomic displacement amplitude of 0.03 Å. In the case of TiS_2, we had to use a larger $5 \times 5 \times 3$ supercell and a larger displacement amplitude of 0.09 Å (see Ref. [19] for details and benchmarks). For the electronic **k** sampling of the reciprocal space, we used Monkhorst-Pack type **k** meshes of $8 \times 8 \times 6$, $4 \times 4 \times 4$, and $2 \times 2 \times 2$ for the primitive cell, $3 \times 3 \times 2$ supercell, and $5 \times 5 \times 3$ supercell, respectively [25]. We also compared the vibrational Γ-point frequencies obtained from CRYSTAL and PHONOPY (see the Supplemental Material [26]). The frequencies are in very good agreement, except for the E_u mode of TiS_2, where the frequencies produced by CRYSTAL and PHONOPY are 115 and 133 cm^{-1}, respectively. The E_u mode also shows the largest error compared with experiment [19], the frequency produced by PHONOPY being closer to the experimental value of 158 cm^{-1} [27].

PHONO3PY code was used to calculate the lattice thermal conductivity and other phonon properties that depend on third-order force constants [28]. PHONO3PY extends the supercell approach of PHONOPY to third-order force constants, which are calculated from supercells with two simultaneously displaced atoms. For all third-order force constant calculations, we applied a $3 \times 3 \times 2$ supercell and the same displacement amplitudes as in the case of second-order force constants.

We investigated the lattice thermal conductivity κ_l using the relaxation time approximation (RTA) for the linearized Boltzmann transport equation. We also studied κ_l and its components with the full solution of the linearized Boltzmann transport equation and this approach is denoted as LBTE from here on [29]. For the phonon **q** sampling of the reciprocal space, we tested **q** meshes up to $30 \times 30 \times 18$ within RTA. With the computationally significantly more demanding LBTE approach, we tested **q** meshes up to $24 \times 24 \times 16$. The results of the RTA convergence tests are illustrated in Fig. 2. κ_l converges rather well for a $20 \times 20 \times 12$ mesh both in the in-plane and cross-plane directions.

The computational costs of calculating the third-order force constants can be decreased by imposing a real-space cutoff distance, beyond which the third-order force constants are set to zero for a triplet of atoms. We systematically tested the real-space cutoff parameter for TiS_2 (see the Supplemental Material [26]). We found that the lattice thermal conductivity of TiS_2 is well converged at 5 Å cutoff. For TiS_2, we did not impose any cutoffs in the final reported calculations. For ZrS_2 and HfS_2, we imposed a cutoff of 6 Å (for comparison, a cutoff of 3.8 Å was applied in a previous study on MoS_2 and WS_2) [30].

The effect of isotope scattering due to the mass variance of natural isotope distributions turned out to be negligible and was not included in the lattice thermal conductivity calculations (see the Supplemental Material [26]).
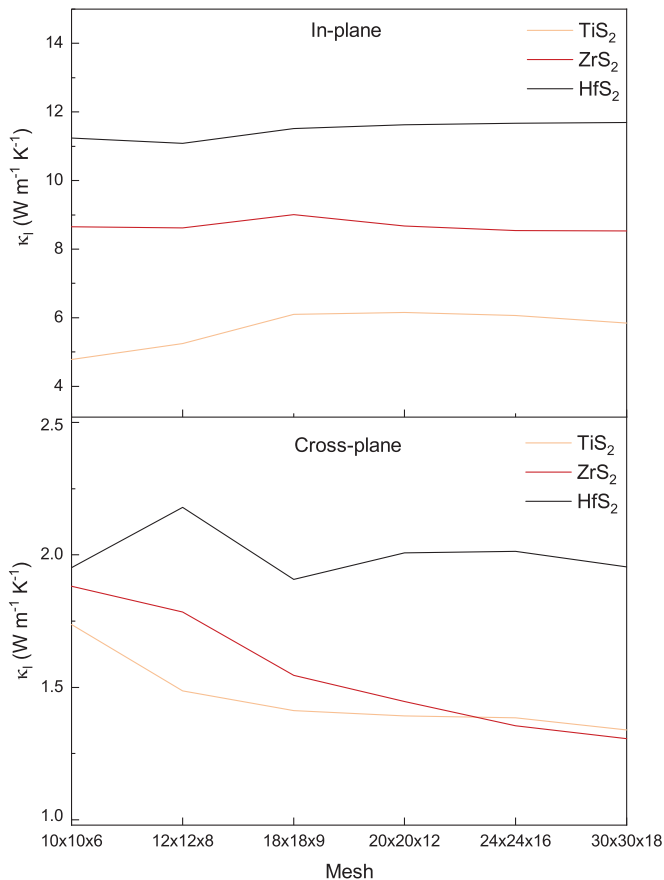
FIG. 2. **q**-mesh convergence test for the lattice thermal conductivity of TiS$_2$, ZrS$_2$, and HfS$_2$ at 300 K (with RTA).

FIG. 3. Lattice thermal conductivity of TiS$_2$, ZrS$_2$, and HfS$_2$ (RTA, $20 \times 20 \times 12$ **q** mesh).

III. RESULTS

A. Lattice thermal conductivity

Within the single-mode relaxation time approximation (RTA), the lattice thermal conductivity tensor can be written as [28]

$$\kappa_l = \frac{1}{NV_0} \sum_{\mathbf{q}j} C_{\mathbf{q}j} v_{\mathbf{q}j} \otimes v_{\mathbf{q}j} \tau_{\mathbf{q}j}, \qquad (2)$$
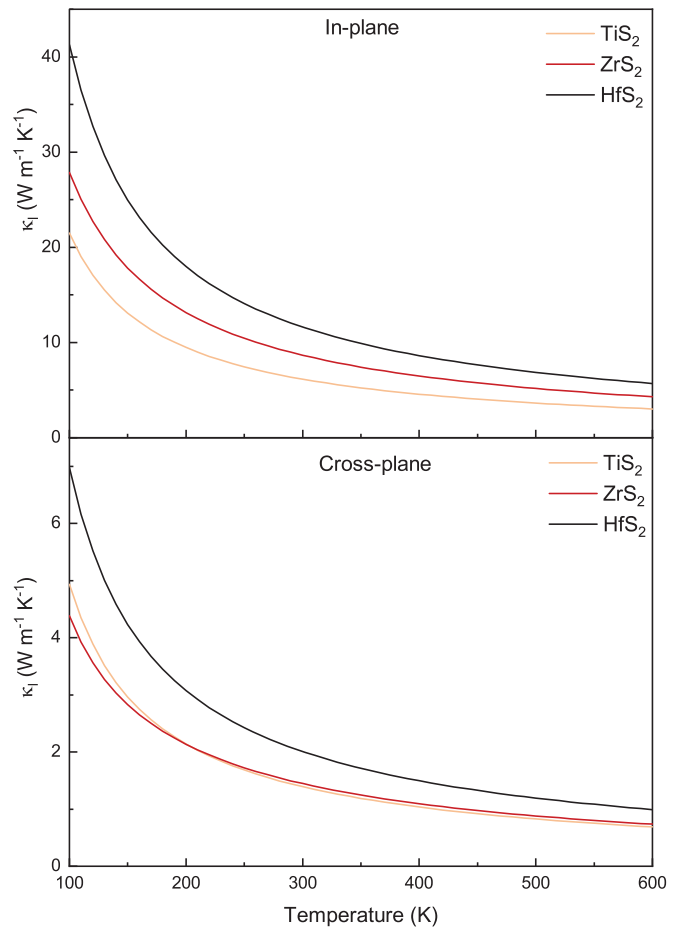
where V_0 is the volume of the unit cell and $C_{\mathbf{q}j}$, $v_{\mathbf{q}j}$, and $\tau_{\mathbf{q}j}$ are the constant volume heat capacity, group velocity, and relaxation time for phonon mode $(\mathbf{q}, j)$, respectively. Within RTA, the phonon relaxation time is equal to phonon lifetime.

Figure 3 shows the in-plane and cross-plane lattice thermal conductivity as a function of temperature for TiS$_2$, ZrS$_2$, and HfS$_2$ (with RTA). The in-plane κ_l decreases in the order HfS$_2 >$ ZrS$_2 >$ TiS$_2$. HfS$_2$ also shows the largest κ_l in the

TABLE I. Lattice thermal conductivity κ_l (W m^{-1} K^{-1}) at 300 K calculated with RTA and LBTE.

	TiS$_2$		ZrS$_2$		HfS$_2$	
	RTA	LBTE	RTA	LBTE	RTA	LBTE
q mesh			In plane			
$18 \times 18 \times 9$	6.1	6.4	9.0	6.2	11.5	10.4
$20 \times 20 \times 12$	6.2	6.4	8.7	10.1	11.6	12.6
$24 \times 24 \times 16$	6.1	6.4	8.5	9.8	11.7	11.5
Expt.	4.5 [1], 6.4 [11], 4.5[a] [5]					
			Cross plane			
$18 \times 18 \times 9$	1.4	1.5	1.5	1.9	1.9	2.0
$20 \times 20 \times 12$	1.4	1.4	1.4	2.0	2.0	2.1
$24 \times 24 \times 16$	1.4	1.4	1.4	1.9	2.0	2.1
Expt.	4.2 [11]					

[a]Measured at 275 K.

cross-plane direction, while κ_l (RTA) for TiS$_2$ and ZrS$_2$ in this direction is practically identical. For all materials, κ_l is clearly larger in the in-plane direction with covalent M–S bonding in comparison to the cross-plane direction with weak interlayer interactions.

Table I shows a comparison of κ_l calculated with RTA and LBTE at 300 K. Experimental data for TiS$_2$ single crystals are also included in the table (corresponding data for ZrS$_2$ and HfS$_2$ are not currently available). With the densest 24 × 24 × 16 **q** mesh, κ_l values obtained with RTA and LBTE are rather similar for TiS$_2$ and HfS$_2$, while in the case of ZrS$_2$ LBTE predicts slightly larger values than RTA. The LBTE values show that κ_l decreases in the order HfS$_2$ > ZrS$_2$ > TiS$_2$ both in the in-plane and cross-plane direction. The in-plane κ_l of TiS$_2$ predicted by LBTE agrees well with the experimental value of Imai *et al.* [11]. At the same time, the LBTE cross-plane value of 1.4 W m^{-1} m^{-1} is clearly smaller than the only available experimental value of 4.2 m^{-1}. In the following sections, we analyze the periodic trends of the calculated κ_l values in more detail.

B. Phonon dispersion relations and cumulative lattice thermal conductivity

A detailed analysis of lattice thermal conductivity can be conducted with the help of cumulative parameters, where the individual elements of lattice thermal conductivity [Eq. (2)] are calculated with respect to the phonon frequency. The results in this and the following sections have been obtained with the LBTE approach at 300 K, using a 20 × 20 × 12 **q** mesh.

Figure 4 shows the phonon dispersion relations of TiS$_2$, ZrS$_2$, and HfS$_2$ together with cumulative lattice thermal conductivity. The in-plane plane κ_l increases steadily as a function of the phonon frequency until the maximum frequency of acoustic phonons in $\Gamma - M$ and $\Gamma - K$ directions of the Brillouin zone is reached. These directions correspond to the *ab* plane in the real space. At the same time, the cross-plane κ_l increases only up to the maximum frequency of $\Gamma - A$ acoustic phonons, corresponding to the cross-plane *c* direction in the real space. The majority of heat in TiS$_2$, ZrS$_2$, and HfS$_2$ is thus carried by acoustic phonons, and the direct contribution of the optical phonons to κ_l is small, in particular for the cross-plane direction. Because the weak van der Waals interaction in the cross-plane direction is rather similar for TiS$_2$, ZrS$_2$ and HfS$_2$, the cross-plane κ_l is also rather similar for all three compounds. In contrast, the interactions in the in-plane direction are governed by the nature of the metal–chalcogen bonding, which is more covalent for TiS$_2$ in comparison to ZrS$_2$ and HfS$_2$ [19]. The differences in the M–S bonding as well as the different atomic masses give rise to differences in the in-plane κ_l for the studied compounds. The phonon dispersion plots also illustrate that HfS$_2$ has a phonon band gap between the acoustic and optical modes, whereas in TiS$_2$ and ZrS$_2$ the acoustic modes cross with the optical modes.

C. Phonon group velocities

We next analyze the individual contributions of $C_{\mathbf{q}j}$, $v_{\mathbf{q}j}$, and $\tau_{\mathbf{q}j}$ to the lattice thermal conductivity [Eq. (2)]. The constant volume heat capacities of the studied compounds are rather similar, even though TiS$_2$ shows a few percent smaller $C_{\mathbf{q}j}$ at temperatures below 500 K (see the Supplemental Material [26]). We will therefore focus on the phonon group velocities and phonon lifetimes in the following analysis. Figure 5 illustrates the cumulative phonon group velocities ($v_{\mathbf{q}j}$) of TiS$_2$, ZrS$_2$, and HfS$_2$. Starting with the in-plane direction, the group velocities of the acoustic modes below 60 cm^{-1} are rather similar for all three compounds, after which differences start to arise. TiS$_2$ shows the highest group velocities, in line with the fact that the Ti–S bonds are the more covalent and the corresponding force constants are also larger. ZrS$_2$ and HfS$_2$ show rather similar cumulative group velocity up until about 125 cm^{-1}, after which the cumulative group velocity of ZrS$_2$ becomes larger. This is in line with the fact that the acoustic modes of HfS$_2$ peak already at about 150 cm^{-1}, while for ZrS$_2$ the highest-energy acoustic modes reach 200 cm^{-1}. As expected, the majority of the cumulative phonon group velocity arises from the acoustic modes and the contributions from the optical modes are clearly smaller for all three compounds.

In the case of the cross-plane direction, the group velocities of the acoustic modes are also rather similar below 60 cm^{-1} for all three compounds. Even for larger frequencies, the differences between the compounds are not large. TiS$_2$ shows the largest cumulative phonon group velocity, followed by ZrS$_2$ and HfS$_2$. Overall, the phonon group velocities in the cross-plane direction are clearly smaller than the group velocities in the in-plane direction. This is expected based on the slopes of the phonon dispersions in the Brillouin zone, as the slope in the $\Gamma - A$ direction (cross plane in real space) is clearly smaller in comparison to the $\Gamma - M$ and $\Gamma - K$ directions (in plane in real space).

D. Grüneisen parameter

We also investigated the phonon mode-dependent Grüneisen parameter $\gamma_{\mathbf{q}j}$ which is a dimensionless measure of anharmonicity of the phonons. In continuum theory, the phonon lifetime $\tau_{\mathbf{q}j}$ is inversely proportional to the square of the averaged Grüneisen parameter, γ^2 [31]. $\gamma_{\mathbf{q}j}$ can be defined as the change of phonon frequency $\omega_{\mathbf{q}j}$ with respect to the change of the volume V:

$$\gamma_{\mathbf{q}j} = -\frac{V}{\omega_{\mathbf{q}j}}\frac{\partial \omega_{\mathbf{q}j}}{\partial V}. \tag{3}$$

Here, $\gamma_{\mathbf{q}j}$ has been obtained directly from the third-order force constants using the relations described in Ref. [32] (pp. 204–205). The calculation of $\gamma_{\mathbf{q}j}$ in PHONO3PY is at the moment limited to systems where the second- and third-order force constants have been obtained for supercells of similar size. As TiS$_2$ required the use of a larger supercell for second-order force constant calculations, Fig. 6 only shows the mode-Grüneisen parameters for ZrS$_2$ and HfS$_2$. A positive value for $\gamma_{\mathbf{q}j}$ means that the frequency of the phonon mode **q**, j decreases when the volume increases. This is the typical behavior of phonon modes as the force constants usually become smaller as the interatomic distances increase. However, some structures such as Cu$_2$O show significant amounts of negative $\gamma_{\mathbf{q}j}$ values, leading in negative thermal expansion in
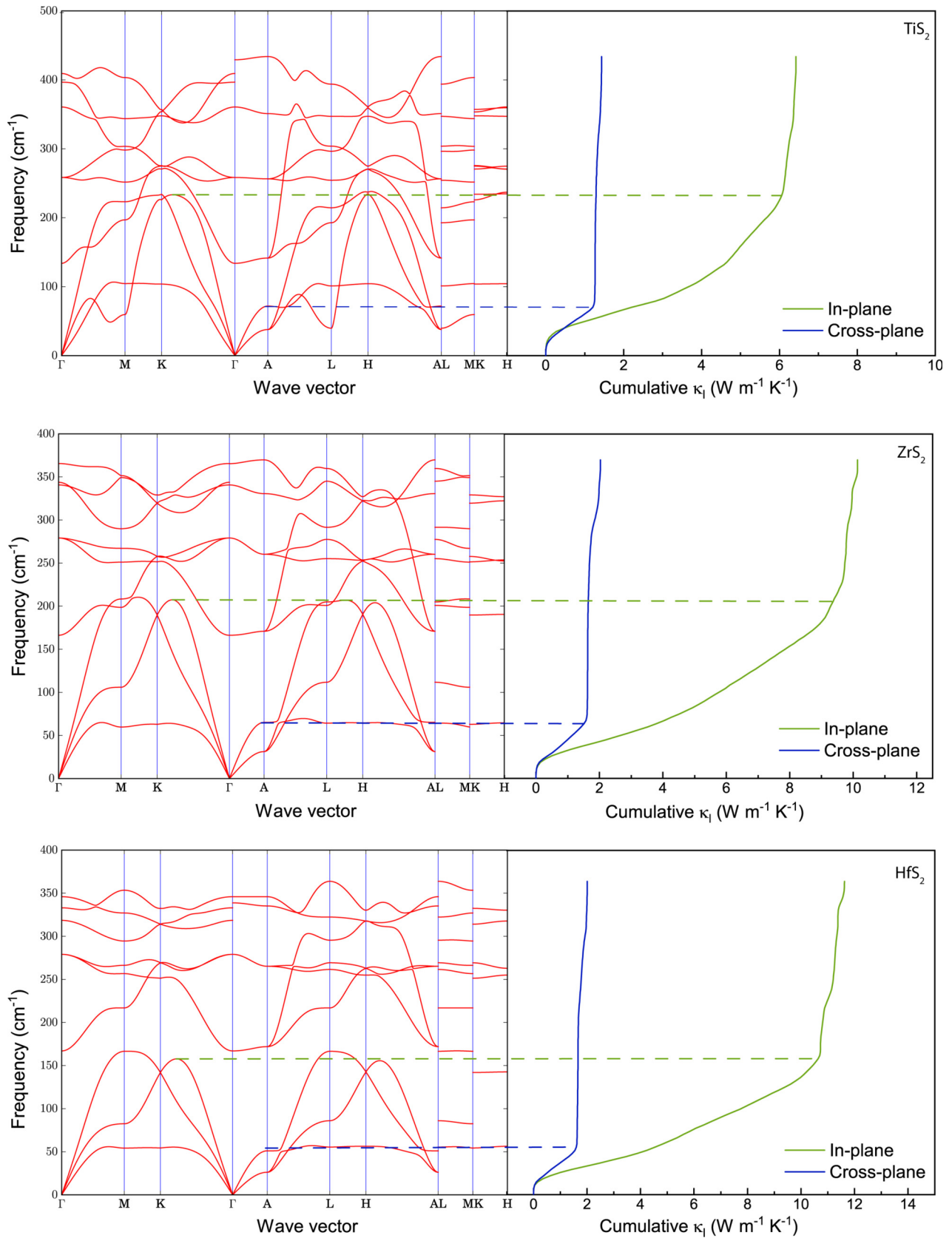
FIG. 4. Phonon dispersion relations and cumulative lattice conductivity κ_l for TiS₂, ZrS₂, and HfS₂. Note that the scale of cumulative κ_l is different for all three materials.
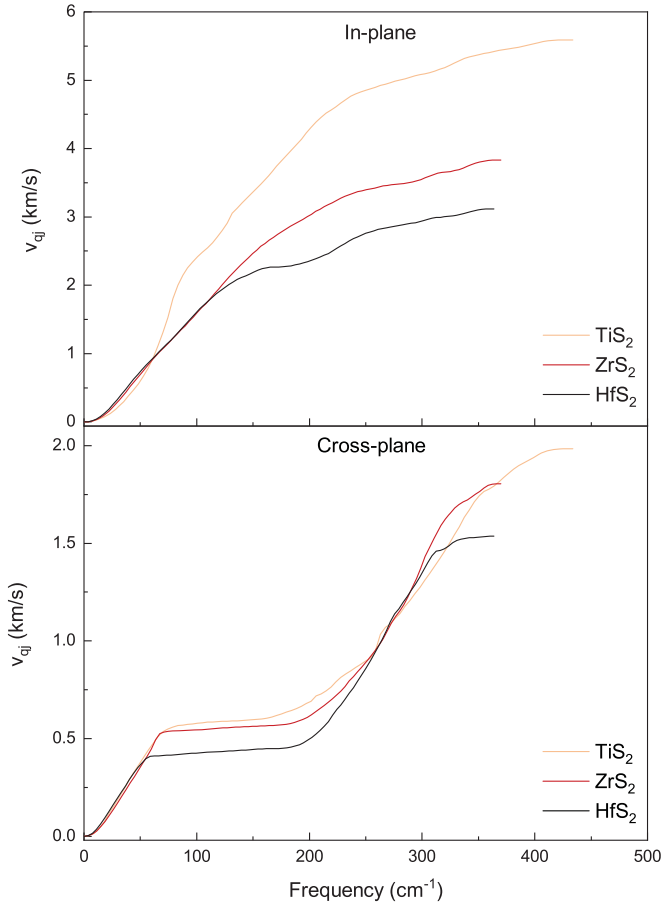
FIG. 5. Cumulative phonon group velocities of TiS$_2$, ZrS$_2$, and HfS$_2$ for in-plane and cross-plane directions.

some temperature range [33]. ZrS$_2$ and HfS$_2$ primarily show positive $\gamma_{\mathbf{q}j}$ values: ZrS$_2$ has few negative $\gamma_{\mathbf{q}j}$ values for low-frequency phonon modes below 50 cm^{-1} and HfS$_2$ has several slightly negative $\gamma_{\mathbf{q}j}$ values at about 50 cm^{-1}. Generally,
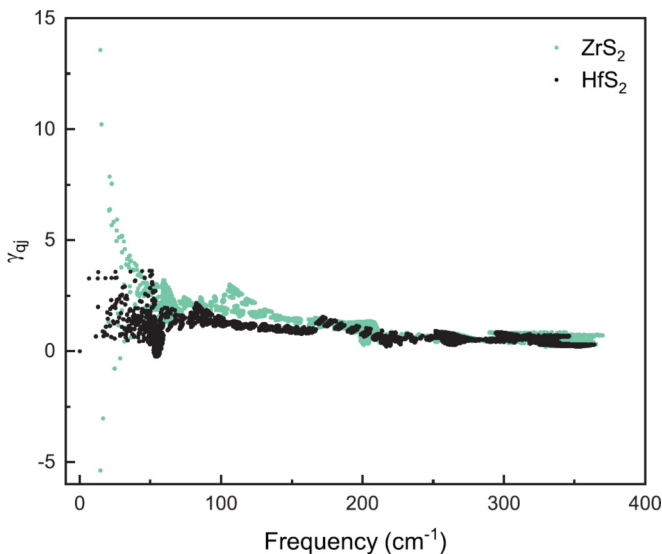

FIG. 6. Mode-Grüneisen parameters $\gamma_{\mathbf{q}j}$ for ZrS$_2$ and HfS$_2$.

the $\gamma_{\mathbf{q}j}$ values are larger for ZrS$_2$ in comparison to HfS$_2$, in particular for acoustic phonon modes below 150 cm^{-1}. This suggests larger phonon anharmonicity in the case of ZrS$_2$.

E. Phonon lifetimes

$\tau_{\mathbf{q}j}$, the lifetime of a phonon mode $\{\mathbf{q}, j\}$, is the only quantity in the formula for lattice thermal conductivity [Eq. (2)] that is directly affected by the phonon anharmonicity. The top part in Fig. 7 shows a cumulative plot of $\tau_{\mathbf{q}j}$ as a function of phonon frequency. From the plot we can see that the cumulative phonon lifetime decreases in the order HfS$_2$ > ZrS$_2$ > TiS$_2$. Shorter phonon lifetimes lead in smaller κ_l values [Eq. (2)] and, in agreement with this, TiS$_2$ with the shortest phonon lifetimes also shows the smallest κ_l.

To better understand the phonon lifetimes of the studied materials, we investigated the imaginary part of phonon self-energy, $\Gamma_{\mathbf{q}j}$. $2\Gamma_{\mathbf{q}j}$ corresponds to the phonon linewidth of phonon mode $\{\mathbf{q}, j\}$ and the phonon lifetime can be obtained as the reciprocal of phonon linewidth [28]:

$$\tau_{\mathbf{q}j} = \frac{1}{2\Gamma_{\mathbf{q}j}}. \qquad (4)$$

The middle panels of Fig. 7 illustrate $\Gamma_{\mathbf{q}j}$ calculated at the M point of the first Brillouin zone [$\mathbf{q} = (0.5, 0.0, 0.0)$], corresponding to in-plane direction in real space. We calculated $\Gamma_{\mathbf{q}j}$ in three different directions and the M point is used as a representative point. The values calculated at different points in different directions are illustrated in the Supplemental Material [26]. The trend of $\Gamma_{\mathbf{q}j}$ values is the same for all studied points: TiS$_2$ shows the largest $\Gamma_{\mathbf{q}j}$ values, leading to shorter phonon lifetimes according to Eq. (4). For ZrS$_2$ and HfS$_2$, the $\Gamma_{\mathbf{q}j}$ values are rather similar, but HfS$_2$ generally shows slightly smaller values for the acoustic modes below 150 cm^{-1}. Even these small differences can lead to differences in the cumulative phonon lifetimes, as ZrS$_2$ and HfS$_2$ show rather different behavior of phonon lifetimes below 150 cm^{-1}.

$\Gamma_{\mathbf{q}j}$ is calculated from the squared three-phonon interaction strength and the weighted joint density of states, w-JDOS [Eq. (11) in Ref. [28]]. w-JDOS describes the three-phonon collision and decay processes as a function of phonon frequency. The collision events refer to three-phonon events, where two interacting phonons are annihilated, creating a third phonon [Eq. (23) in Ref. [28]]. In the case of a decay event, one phonon is annihilated and two phonons are created [Eq. (24) in Ref. [28]]. Both types of events, weighted by phonon mode occupations, are taken into account in the calculation of w-JDOS and eventually in the calculation of $\Gamma_{\mathbf{q}j}$.

Room-temperature w-JDOS at the M point of the first Brillouin zone [$\mathbf{q} = (0.5, 0.0, 0.0)$] is presented in the bottom panels of Fig. 7. The w-JDOS values calculated at different points in the reciprocal space are illustrated in the Supplemental Material [26]. In all three materials, the collision events dominate starting from about 300 cm^{-1}. From the point of view of phonon dispersions, a phonon band gap between acoustic and optical phonons opens up when moving from Ti to Hf. The opening of such phonon band gap could affect the number of possible three-phonon interactions between acoustic and optical phonons, reducing phonon-phonon scattering and increasing phonon lifetimes. However, the w-JDOS
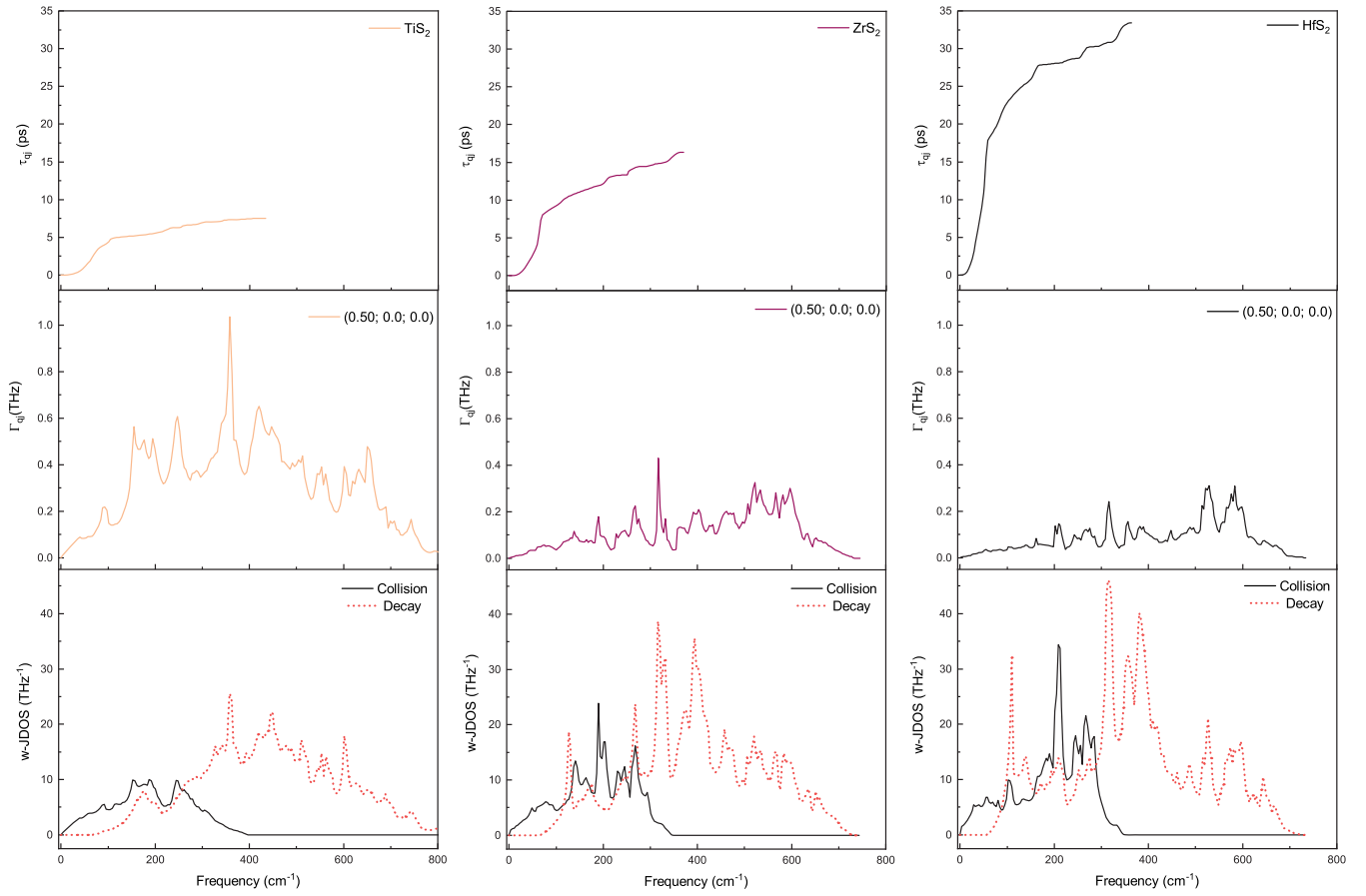
FIG. 7. Cumulative phonon lifetime $\tau_{\mathbf{q}j}$, imaginary part of self-energy $\Gamma_{\mathbf{q}j}$, and weighted joint density of states (w-JDOS) for TiS₂, ZrS₂, and HfS₂ as a function of phonon frequency. $\Gamma_{\mathbf{q}j}$ and w-JDOS are presented for the M point of the first Brillouin zone [$\mathbf{q} = (0.5, 0.0, 0.0)$]. For w-JDOS, solid lines correspond to collision events and dashed lines to decay events (see text).

plots of ZrS₂ and HfS₂ do not show significant differences for frequencies below 100 cm⁻¹, where the differences in phonon lifetimes arise. This suggests that the smaller $\Gamma_{\mathbf{q}j}$ of HfS₂ is determined by the three-phonon interaction strength, which in turn is calculated from the third order force constants and harmonic phonon properties. As discussed above, the mode-Grüneisen parameters for acoustic phonon modes below 150 cm⁻¹, calculated directly from the third order force constants, are larger for ZrS₂ in comparison to HfS₂. This suggests that the slightly larger phonon anharmonicity in ZrS₂ results in shorter phonon lifetimes and smaller κ_l in comparison to HfS₂.

F. Thermoelectric figure of merit

We now investigate the thermoelectric figure of merit ZT for n-type TiS₂, ZrS₂, and HfS₂ by combining the lattice thermal conductivity results obtained here with the previously calculated band-structure dependent quantities of Eq. (1) (S, σ, κ_e) [19]. Room-temperature ZT as a function of carrier concentration (doping) is illustrated in Fig. 8. Among the studied materials, TiS₂ shows the largest ZT values both in the in-plane and cross-plane directions. For all three materials, the maximum ZT in the cross-plane direction is larger than in the in-plane direction. Since there are no experimental values available for ZrS₂ and HfS₂, we focus on TiS₂ in the fol-

lowing comparisons to experiments. In the in-plane direction, maximum ZT value of 0.08 is reached at a carrier concentration of 1.4×10^{20} cm⁻³. In an experimental study on TiS₂ single crystals, Koumoto *et al.* reported room-temperature ZT of 0.06 ± 0.01 at a carrier concentration of 3.4×10^{20} cm⁻³.
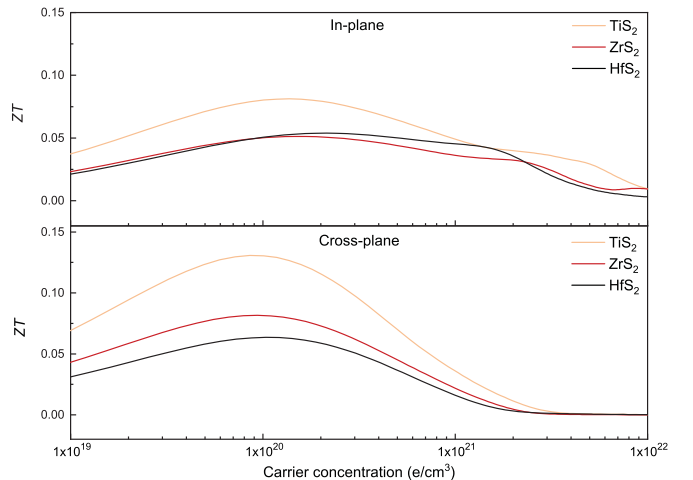

FIG. 8. Thermoelectric figure of merit ZT for TiS₂, ZrS₂, and HfS₂ at 300 K.

For comparison, Imai *et al.* reported clearly larger ZT of 0.16 at a carrier concentration of 2.8×10^{20} cm^{-3} [11].

IV. CONCLUSION

We have combined the dispersion-corrected hybrid DFT method with the Boltzmann transport equation to investigate the periodic trends in the lattice thermal conductivity κ_l of layered group 4 disulfides TiS$_2$, ZrS$_2$, and HfS$_2$. The use of dispersion corrections is important for the proper description of the interlayer van der Waals interactions. We used both relaxation time approximation and the full solution of linearized BTE, showing that for these materials κ_l is described rather well already at the RTA level of theory. Analysis of cumulative κ_l showed that the majority of heat is carried by acoustic phonons. The in-plane κ_l decreases as HfS$_2$ > ZrS$_2$ > TiS$_2$. Even though the phonon group velocity of acoustic phonons in TiS$_2$ is higher in comparison to ZrS$_2$ and HfS$_2$ the signif-

icantly shorter phonon lifetime in TiS$_2$ results in the smallest in-plane κ_l within the three materials. Analysis of mode-Grüneisen parameters shows ZrS$_2$ to possess slightly larger phonon anharmonicity and consequently shorter phonon lifetimes in comparison to HfS$_2$. The predicted in-plane κ_l of TiS$_2$ is in reasonable agreement with the experimental literature values, while in the case of ZrS$_2$ and HfS$_2$ the predicted values can be compared with future experiments. TiS$_2$ shows the most promising overall thermoelectric performance among the studied materials, both in cross-plane and in-plane direction.

ACKNOWLEDGMENTS

[1] C. Wan, X. Gu, F. Dang, T. Itoh, Y. Wang, H. Sasaki, M. Kondo, K. Koga, K. Yabuki, G. J. Snyder *et al.*, Flexible n-type thermoelectric materials by organic intercalation of layered transition metal dichalcogenide TiS$_2$, Nat. Mater. **14**, 622 (2015).

[2] C. Wan, R. Tian, M. Kondou, R. Yang, P. Zong, and K. Koumoto, Ultrahigh thermoelectric power factor in flexible hybrid inorganic-organic superlattice, Nat. Commun. **8**, 1024 (2017).

[3] C. Wan, Y. Wang, N. Wang, W. Norimatsu, M. Kusunoki, and K. Koumoto, Intercalation: Building a natural superlattice for better thermoelectric performance in layered chalcogenides, J. Electron. Mater. **40**, 1271 (2011).

[4] J. Zhang, X. Y. Qin, H. X. Xin, D. Li, and C. J. Song, Thermoelectric properties of Co-doped TiS$_2$, J. Electron. Mater. **40**, 980 (2011).

[5] R. Daou, H. Takahashi, S. Hébert, M. Beaumale, E. Guilmeau, and A. Maignan, Intrinsic effects of substitution and intercalation on thermal transport in two-dimensional TiS$_2$ single crystals, J. Appl. Phys. **117**, 165101 (2015).

[6] G. Guelou, P. Vaqueiro, J. Prado-Gonjal, T. Barbier, S. Hebert, E. Guilmeau, W. Kockelmann, and A. V. Powell, The impact of charge transfer and structural disorder on the thermoelectric properties of cobalt intercalated TiS$_2$, J. Mater. Chem. C **4**, 1871 (2016).

[7] C. Wan, Y. Wang, N. Wang, W. Norimatsu, M. Kusunoki, and K. Koumoto, Development of novel thermoelectric materials by reduction of lattice thermal conductivity, Sci. Technol. Adv. Mater. **11**, 044306 (2010).

[8] D. Li, X. Qin, J. Zhang, L. Wang, and H. Li, Enhanced thermoelectric properties of bismuth intercalated compounds Bi$_x$TiS$_2$, Solid State Commun. **135**, 237 (2005).

[9] M. Ohta, S. Satoh, T. Kuzuya, S. Hirai, M. Kunii, and A. Yamamoto, Thermoelectric properties of Ti$_{1+x}$S$_2$ prepared by CS2 sulfurization, Acta Mater. **60**, 7232 (2012).

[10] S. Hébert, D. Berthebaud, R. Daou, Y. Bréard, D. Pelloquin, E. Guilmeau, F. Gascoin, O. Lebedev, and A. Maignan, Searching

for new thermoelectric materials: Some examples among oxides, sulfides and selenides, J. Phys.: Condens. Matter **28**, 013001 (2016).

[11] H. Imai, Y. Shimakawa, and Y. Kubo, Large thermoelectric power factor in TiS$_2$ crystal with nearly stoichiometric composition, Phys. Rev. B **64**, 241104(R) (2001).

[12] G. Ding, J. Chen, K. Yao, and G. Gao, Convergence of separate orbits for enhanced thermoelectric performance of layered ZrS$_2$, New J. Phys. **19**, 073036 (2017).

[13] H. Lv, W. Lu, D. Shao, H. Lu, and Y. Sun, Strain-induced enhancement in the thermoelectric performance of a ZrS$_2$ monolayer, J. Mater. Chem. C **4**, 4538 (2016).

[14] H. Y. Lv, W. J. Lu, X. Luo, H. Y. Lu, X. B. Zhu, and Y. P. Sun, Enhancing the thermoelectric performance of a HfS$_2$ monolayer through valley engineering, arXiv:1608.05464.

[15] G. Yumnam, T. Pandey, and A. K. Singh, High temperature thermoelectric properties of Zr and Hf based transition metal dichalcogenides: A first principles study, J. Chem. Phys. **143**, 234704 (2015).

[16] R. Dovesi, R. Orlando, A. Erba, C. M. Zicovich-Wilson, B. Civalleri, S. Casassa, L. Maschio, M. Ferrabone, M. De La Pierre, P. D'Arco, Y. Noël, M. Causà, M. Rérat, and B. Kirtman, CRYSTAL14: A program for the *ab initio* investigation of crystalline solids, Int. J. Quantum Chem. **114**, 1287 (2014).

[17] C. Adamo and V. Barone, Toward reliable density functional methods without adjustable parameters: The PBE0 model, J. Chem. Phys. **110**, 6158 (1999).

[18] F. Weigend and R. Ahlrichs, Balanced basis sets of split valence, triple zeta valence and quadruple zeta valence quality for H to Rn: Design and assessment of accuracy, Phys. Chem. Chem. Phys. **7**, 3297 (2005).

[19] N. Glebko, I. Aleksandrova, G. C. Tewari, T. S. Tripathi, M. Karppinen, and A. J. Karttunen, Electronic and vibrational properties of TiS$_2$, ZrS$_2$, and HfS$_2$: Periodic trends studied by dispersion-corrected hybrid density functional methods, J. Phys. Chem. C **122**, 26835 (2018).

[20] S. Grimme, J. Antony, S. Ehrlich, and H. Krieg, A consistent and accurate *ab initio* parametrization of density functional dispersion correction (DFT-D) for the 94 elements H-Pu, J. Chem. Phys. **132**, 154104 (2010).

[21] S. Grimme, S. Ehrlich, and L. Goerigk, Effect of the damping function in dispersion corrected density functional theory, J. Comput. Chem. **32**, 1456 (2011).

[22] A. Togo, F. Oba, and I. Tanaka, First-principles calculations of the ferroelastic transition between rutile-type and CaCl₂-type SiO₂ at high pressures, Phys. Rev. B **78**, 134106 (2008).

[23] A. Togo and I. Tanaka, First principles phonon calculations in materials science, Scr. Mater. **108**, 1 (2015).

[24] A. Erba, M. Shahrokhi, R. Moradian, and R. Dovesi, On how differently the quasi-harmonic approximation works for two isostructural crystals: Thermal properties of periclase and lime, J. Chem. Phys. **142**, 044114 (2015).

[25] H. J. Monkhorst and J. D. Pack, Special points for Brillouin-zone integrations, Phys. Rev. B **13**, 5188 (1976).

[26] See Supplemental Material at http://link.aps.org/supplemental/10.1103/PhysRevB.100.024301 which includes additional information on calculations for phonon interaction cutoffs, isotope scattering, constant volume heat capacities, imaginary part of phonon self-energy, and weighted joint phonon density of states.

[27] H. P. Vaterlaus and F. Levy, Phonons and free carriers in group IVb transition-metal dichalcogenides, J. Phys. C **18**, 2351 (1985).

[28] A. Togo, L. Chaput, and I. Tanaka, Distributions of phonon lifetimes in Brillouin zones, Phys. Rev. B **91**, 094306 (2015).

[29] L. Chaput, Direct Solution to the Linearized Phonon Boltzmann Equation, Phys. Rev. Lett. **110**, 265506 (2013).

[30] D. O. Lindroth and P. Erhart, Thermal transport in van der Waals solids from first-principles calculations, Phys. Rev. B **94**, 115205 (2016).

[31] J. M. Ziman, *Electrons and Phonons: The Theory of Transport Phenomena in Solids* (Oxford University Press, Oxford, 1960).

[32] D. Wallace, *Thermodynamics of Crystals* (Dover, Mineola, NY, 1990).

[33] J. Linnera and A. J. Karttunen, *Ab initio* study of the lattice thermal conductivity of Cu₂O using the generalized gradient approximation and hybrid density functional methods, Phys. Rev. B **96**, 014304 (2017).